Appl. Magn. Reson. 31, 627–647 (2007)

Applied Magnetic Resonance

Radio Frequencies in EPR: Conventional and Advanced Use

I. A. Gromov and **J. Harmer**

Laboratory of Physical Chemistry, Department of Chemistry and Applied Biosciences, ETH Zürich, Zürich, Switzerland

Received August 14, 2006; revised September 14, 2006

Abstract. This mini-review focuses on various aspects of the application of radio frequency (rf) irradiation in electron paramagnetic resonance (EPR). The development of the electron–nuclear double resonance (ENDOR) technique is briefly described, and we highlight the use of circularly polarized rf fields and pulse ENDOR methodology in one- and two-dimensional experiments. The capability of pulse ENDOR at Q-band is illustrated with interesting experimental examples. Electron spin echo envelope modulation effects induced by an rf field in liquid samples demonstrate another role which rf fields can play. Technical achievements in the design of ENDOR resonators are illustrated by the example of a bridged loop-gap resonator. Finally, the influence of longitudinal rf fields on the dynamics of EPR transitions is explained using a dressed spin resonance treatment.

1 Introduction

One of the widely adopted strategies in spectroscopy is to use irradiation at multiple frequencies in order to increase the quality of the information obtained. A prominent example is electron–nuclear double resonance (ENDOR), which was introduced fifty years ago [1]. ENDOR combines in an optimal way the high sensitivity of electron paramagnetic resonance (EPR) with the high resolution of nuclear magnetic resonance (NMR). In the continuous-wave (cw) variant the effect manifests itself when a saturated electron spin transition is desaturated by driving an associated nuclear spin transition with a radio frequency (rf) field. In the pulse version [2, 3], the polarization of an EPR transition is manipulated stepwise in time. In the first step it is inverted by driving an electron spin transition with a microwave (mw) pulse(s), then the polarization of this EPR transition is altered by an rf pulse if it is on resonance with a nuclear transition. The change due to the latter process is monitored via an electron spin echo.

However, ENDOR is not only an effect that can be observed by probing paramagnetic species with mw and rf irradiation. For instance, an electron spin resonance was recently observed at rf on electron spins dressed with a strong mw field [4]. Alternatively, the EPR transition probability can be manipulated by

dressing the electron spins with an rf field [5]. A popular pulse technique competing with ENDOR, but nevertheless complementary, is the electron spin echo envelope modulation (ESEEM) method [6]. In this technique the local magnetic field at the nucleus is altered through electron spin flips and the following precession of the nuclear spins is monitored via an electron spin echo. The method requires a nonzero coupling element between the nuclear Zeeman states, i.e., an anisotropic hyperfine interaction (hfi). For the latter reason there is no ESEEM effect in liquids, where the hfi anisotropy is averaged out (for the $S = 1/2$ system). Nevertheless, the required nonsecular coupling can be created artificially by linking nuclear Zeeman states with an rf field resonant with a nuclear transition [7].

In this mini-review we describe, not claiming to be general or complete, the evolution of the ENDOR methodology and other rf-based techniques at the ETH Zürich that were developed by Arthur Schweiger (who passed away on January 4, 2006) and his colleagues. The use of conventional and advanced pulse double resonance methods to characterize complex biological systems or small novel molecules is taken for illustrations.

2 ENDOR with Circularly Polarized Fields

Since its discovery, cw ENDOR has been increasingly used in the structural determination of free radicals and transition metal complexes. The effect has been studied in great detail theoretically and experimentally [8–10]. Transition probabilities, the hyperfine enhancement effect, and related relaxation mechanisms were studied to optimize and develop the method.

One of the problems that investigators faced immediately is that in complex systems with a large number of interacting nuclei the high density of spectral lines complicates or prevents the interpretation of an ENDOR spectrum. Although the number of lines in an ENDOR spectrum increases in an additive way with the number of nuclei, the overlap of spectral lines from different nuclei, the second-order splittings, and dipole–dipole nuclear interactions, etc., seriously decrease the resolution capability of the method. To reduce the number of lines in an ENDOR spectrum, Schweiger and Günthard proposed the use of circularly polarized (CP) rf fields [11]. The basic idea exploits the sense of rf field rotation to separate different contributions in the spectrum. The CP rf field can be produced using two mutually orthogonal half-loop coils driven equally by two rf amplifiers in quadrature [12]. The polarization-dependent transition probability has been analyzed using first-order Rayleigh–Schrödinger perturbation theory and analytical solutions have been obtained with the Bleaney–Bir approach [13]. Practical formulas were derived for the relative transition probabilities (enhancement factors) for CP fields. They are given in Table 1 (adapted from ref. 13) for the two-spin electron-nuclear system $S = 1/2$ and $I = 1/2$, which we use in the following to explain the phenomenon. For the sake of simplicity, the nuclear g-factor and Fermi contact term a are taken as positive. The hyperfine dipolar coupling is $\mathbf{T} = (-T, -T, 2T)$, so that $\mathbf{A} = a\mathbf{E} + \mathbf{T}$ and $A_{\parallel} = a + 2T$, $A_{\perp} = a - T$.

Table 1. Relative transition probabilities for circularly polarized rf fields.[a]

Hfi and circulating rotation[b]	$m_S = 1/2$		$m_S = -1/2$	
1	$a_{iso} < 2\omega_I$	$a_{iso} > 2\omega_I$		
σ^+	0	ε_1^-	0	
σ^-	ε_1^-	0	ε_1^+	
2	$A_\parallel < 2\omega_I$	$A_\parallel > 2\omega_I$		
σ^+	0	ε_2^+	0	
σ^-	ε_2^+	0	ε_2^-	
3			$A_\parallel < 2\omega_I$	$A_\parallel > 2\omega_I$
σ^+	ε_3		ε_3	ε_4^+
σ^-	ε_4^-		ε_4^+	ε_3

[a] The $\varepsilon_i^\pm$ are enhancement factors. $\varepsilon_1^\pm = (1 \pm a/2\omega_I)^2$, $\varepsilon_2^\pm = (1 \pm A_\parallel/4\omega_I)^2$, $\varepsilon_3 = (3A_\parallel/8\omega_I)^2$, $\varepsilon_4^\pm = (1 \pm A_\parallel/8\omega_I)^2$.

[b] $\sigma^\mp$ denotes left or right-hand circulating irradiation. Hfi for $S = 1/2$, $I = 1/2$ is (1) isotropic, $a > 0$; (2) dipolar, $\mathbf{B}_0 \parallel \mathbf{A}_\parallel$; (3) dipolar, $\mathbf{B}_0 \parallel \mathbf{A}_\perp$.

The electron g-factor is taken as that for a free electron. When the hyperfine coupling is isotropic (or the magnetic field $\mathbf{B}_0 \parallel \mathbf{A}_\parallel$) and the coupling is weak, a, $A_\parallel < 2\omega_I$, the transitions in both electron spin manifolds m_S are observed with a left-hand (σ^-) rotating rf field only. In the strong coupling case, a, $A_\parallel > 2\omega_I$, transitions in the $m_S = 1/2$ manifold are observed with a right-hand rotating rf field (σ^+), and the transitions in the $m_S = -1/2$ manifold with a left-hand rotating rf field. When the static magnetic field is perpendicular to the axis $\mathbf{A}_\parallel$ ($\mathbf{B}_0 \perp \mathbf{A}_\parallel$) the correspondence is still the same: weak coupling gives ($m_S = \pm 1/2 \rightarrow \sigma^-$) and strong coupling ($m_S = \pm 1/2 \rightarrow \sigma^\pm$). Note that other combinations appear with probability $(3A_\parallel/8\omega_I)^2$, which can be neglected for weakly coupled high-g_n nuclei.

A practical example of CP-ENDOR is illustrated in Fig. 1 by the copper complex $[Cu(dien)(bipyam)][NO_3]_2$ [10]. There are four ^{14}N nuclei coupled to copper and the complex has two magnetically nonequivalent sites (32 transitions in total). In addition, there are proton contributions in the spectrum below about 19 MHz. As a result, the ENDOR spectrum is very crowded even for a single crystal (Fig. 1a). CP-ENDOR employing a right-hand polarized rf field considerably simplifies the spectrum which shows 16 resonance lines from the strongly coupled nitrogens of two sites for the one spin manifold with $m_S A > 0$ only (Fig. 1b). Further selectivity was achieved with a CP-DOUBLE ENDOR experiment [14]. This is a special version of the triple ENDOR experiment [15], which utilizes a combination of linearly and circularly polarized rf fields. In this experiment the intensity change of a particular nuclear transition is observed with a linearly polarized rf field, while the frequency of the circularly polarized rf field is swept. Only nuclei having an energy level in common and belonging to the selected electron spin manifold give a contribution to the spectrum. This is illustrated in Fig. 1c for the above mentioned copper complex. The CP-DOUBLE ENDOR spectrum obtained with linearly and right-hand circularly polarized rf

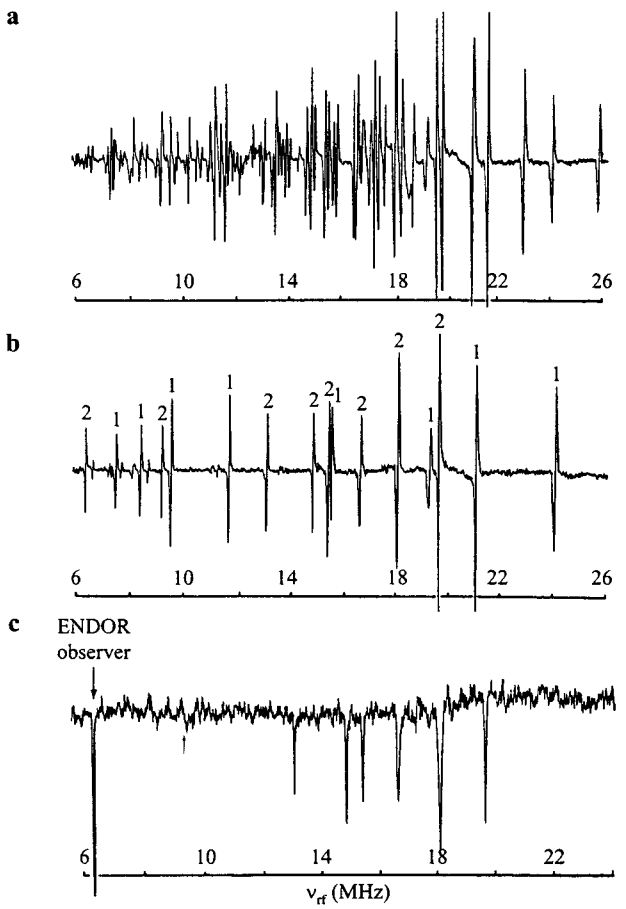

Fig. 1. ENDOR spectra of a $[Cu(dien)(bipyam)][NO_3]_2$ single crystal at an arbitrary orientation. **a** The crowded conventional ENDOR spectrum containing all possible contributions of two sets of four nonequivalent nitrogens and a large number of protons; **b** CP-ENDOR spectrum measured with an rf field rotating in right-hand sense. Nitrogen transitions with $m_S A > 0$ from the two sites, 1 and 2, are visible in the spectrum; and **c** CP-DOUBLE ENDOR. The transition at 6.4 MHz was monitored with a linearly polarized rf field as a function of the frequency of a right-hand CP rf field. The spectrum consists of the eight transitions of site 2 with $m_S A > 0$. The smaller arrow marks the transition which becomes visible at other observer positions (adapted from ref. 10).

fields consists only of eight nitrogen lines from a single site with $m_S A > 0$. Further development in this direction resulted in a two-dimensional (2-D) technique based on polarization-modulated ENDOR [16].

Several additional methods have also been introduced to improve the spectral resolution. In a nuclear spin decoupling experiment the broadening and splitting due to nuclear dipole–dipole coupling of proton pairs was suppressed by pumping one of the nuclear transitions [17]. A resolution improvement in ENDOR

can also be achieved by monitoring multiple-quantum (n-photon) transitions which have a line width inversely proportional to n [18]. In the latter case, one or two rf fields have been used to observe the effect in an $I = 1$ system by exploiting the inequality of the nuclear energy level spacing to enhance two-photon transitions. 2-D nuclear-Zeeman correlated cw ENDOR was developed by using the properties of a combination of B_0 field modulation and rf frequency modulation [19]. An overview of the development of ENDOR spectroscopy in this area can be found in ref. 10.

3 Pulse ENDOR Methodology

At the end of the 1970s, EPR spectroscopy underwent the next innovative advance. Pulse EPR methods became widely used in natural sciences. The characteristic sentence from that time was "the spectroscopist who rubs this Alladin's lamp there now opens up the mysterious world of spin acrobatics with its many novel and surprising phenomena" [20]. Indeed, the development of ESEEM techniques and pulse ENDOR have opened a new perspective in ligand hyperfine spectroscopy, in particular for disordered systems.

Pulse excitation opened many possibilities to manipulate the state of a spin ensemble. To describe the new methodology, the theoretical approach used in pulse NMR, where the density operator is expressed in terms of product operators, was adapted [21]. This elegant approach has been applied to pulse ENDOR as well and provides a basis for its further development [22]. To illustrate this approach, let us take a simple example – the evolution of polarization during a pulse ENDOR experiment. Consider the two-spin electron-nuclear system $S = 1/2$ and $I = 1/2$ with the states $|\beta\alpha\rangle$, $|\beta\beta\rangle$, $|\alpha\beta\rangle$ and $|\alpha\alpha\rangle$, where the first index denotes the electron spin state and the second the nuclear spin state. In the product operator formalism an evolution of the spin density operator during the Davies ENDOR pulse sequence [3] can be expressed for the $|\beta\alpha\rangle \rightarrow |\alpha\alpha\rangle$ EPR transition resonant with a selective mw pulse as follows [22]:

$$
\begin{aligned}
-S_z &= -S_z I^\alpha - S_z I^\beta \xrightarrow{\pi S_x I^\alpha} S_z I^\alpha - S_z I^\beta \\
&= 2S_z I_z \xrightarrow{\gamma S^\alpha I_x} 2S_z I_z \frac{(1+\cos\gamma)}{2} - I_z \frac{(1-\cos\gamma)}{2} - S^\alpha I_y \sin\gamma \\
&\xrightarrow{(\pi/2)S_x I^\alpha} \xrightarrow{\mathcal{H}_0\tau} \xrightarrow{\pi S_x I^\alpha} \xrightarrow{\mathcal{H}_0\tau} S_y I^\alpha \frac{(1+\cos\gamma)}{2} + \ldots ,
\end{aligned}
\qquad (1)
$$

where γ is the turning angle of the rf pulse and the spin operators belong to the mixed base set of the product operators for an electron-nuclear pair [22]. The base operators have relevant spectroscopic meaning. The sequence above starts with an equal polarization of the two electron transitions $-S_z I^\alpha - S_z I^\beta$, and then the polarization of one EPR transition is inverted by a π-pulse applied along the

x-axis, $S_zI^\alpha - S_zI^\beta$. An rf pulse acting on the nuclear transition in the α electron spin manifold reduces this polarization by a factor $(1 + \cos\gamma)/2$, restores the equivalence in polarization of the nuclear transitions $-I_z(1 - \cos\gamma)/2$, and creates nuclear coherence $-S^\alpha I_y \sin\gamma$. The polarization changes are read out with the $\pi/2$-τ-π primary echo sequence applied to the same electron transition resulting in the creation of electron coherence. Detection gives $\mathrm{Tr}\{S_yI^\alpha(-S_y)(1 + \cos\gamma)/2\} = -(1 + \cos\gamma)/4$. For $\gamma = \pi$ the polarization transfer is optimal and the electron spin echo intensity is reduced to zero. Thus the ENDOR efficiency is 1/2. A similar result can be derived for the $|\beta\beta\rangle \rightarrow |\alpha\beta\rangle$ EPR transition. The efficiency of 1/2 occurs in the ideal case since the rf pulse inverts the polarization in one electron spin manifold only.

A selective mw pulse affects the polarization of both nuclear transitions, but a selective monochromatic rf pulse does not, because the ENDOR frequencies, ω_α for $|\alpha\alpha\rangle \rightarrow |\alpha\beta\rangle$ and ω_β for $|\beta\alpha\rangle \rightarrow |\beta\beta\rangle$, are different. Two rf frequencies resonant with ω_α and ω_β can be used to invert nuclear polarization in both m_S electron spin manifolds

$$2S_zI_z \xrightarrow{\gamma S^\alpha I_x} \xrightarrow{\gamma S^\beta I_x} 2S_zI_z\cos\gamma. \tag{2}$$

However, the frequency of the second nuclear transition is generally not known in advance, making this approach impossible to implement. An exception occurs in liquid samples with isotropic couplings since the relationship between the two nuclear transition frequencies is known [23]. In the case of weak coupling, the frequencies are symmetrically placed with respect to the nuclear Larmor frequency and the condition for Eq. (2) is fulfilled by sweeping two rf frequencies symmetrically in opposite directions with respect to the Larmor frequency. Recently a pulse version of this special TRIPLE experiment was successfully applied in the solid state at W-band [24] where asymmetries in the nuclear frequencies are frequently small because the nuclear Zeeman contribution dominates over the hfi.

Alternatively, it is possible to use the same m_S spin manifold to invert both nuclear polarizations. Firstly, the nuclear polarization is inverted in a certain m_S manifold, then the states of the two m_S manifolds are exchanged using a non-selective mw π-pulse, and finally the polarization in the same m_S manifold is inverted again. This implies that the second pulse in Eq. (2) can be replaced with a composite pulse as follows [22]:

$$\xrightarrow{\gamma S^\beta I_x} = \xrightarrow{\pi S_x} \xrightarrow{\gamma S^\alpha I_x} \xrightarrow{\pi S_x}, \tag{3}$$

which produces

$$2S_zI_z \xrightarrow{\gamma S^\alpha I_x} \xrightarrow{\pi S_x} \xrightarrow{\gamma S^\alpha I_x} -2S_zI_z\cos\gamma. \tag{4}$$

The last pulse in Eq. (3) was skipped because it just inverts the signal (brings the nuclear polarization back to its "native" manifold). Comparing the second

row in Eqs. (1) and (4) we conclude that an efficiency of 1 is realized in the latter case [22].

Different overlapping contributions in an ENDOR spectrum can potentially be disentangled by expanding into a second dimension. This is possible with the Mims ENDOR sequence, where the polarization pattern depends on the delay τ in the polarization generator $\pi/2_{mw}$-τ-$\pi/2_{mw}$ of the sequence $\pi/2_{mw}$-τ-$\pi/2_{mw}$-π_{rf}-$\pi/2_{mw}$-τ-echo. The echo intensity is proportional to $1 + \cos A\tau$ and thus the ENDOR spectrum can be disentangled into a hyperfine dimension by incrementing the τ value. The resolution is however often limited as the oscillations in the τ-domain decay quickly with the phase memory time T_m and the polarization grating vanishes. But when the hyperfine frequencies are larger than the decay rate $1/T_m$ the method works, as, for example, with the [Rh(tropp^{ph})$_2$] radical where a two-dimensional Mims ENDOR experiment allowed the rhodium contribution to be separated [25].

Another ingenious approach makes use of the generation of nuclear coherence (NC) and its evolution in time. In a hyperfine-correlated ENDOR (HYEND) experiment [26] the hyperfine coupling is monitored as the difference between nuclear frequencies in the two electron spin manifolds. The pulse sequence for the HYEND experiment and the time evolution of the spin states are shown in Fig. 2 (adapted from ref. 27). The NC created by $(\pi)_{mw}$-$(\pi/2)_{rf}$ in the α electron spin manifold at step 2 has the frequency of the resonant rf field, $\omega_\alpha = \omega_{rf}$. The NC is then immediately transferred to the β electron spin manifold by a non-selective mw π-pulse, where it evolves for a time T at frequency ω_β, and is then transferred back to the α electron spin manifold. The following rf $\pi/2$-pulse converts the coherence to polarization at step 5, which is finally monitored via a two-pulse echo. The polarization at position 5 depends on the phase difference accumulated by the NC with respect to the rf during its evolution in the β electron spin manifold. This difference is $|\omega_\alpha - \omega_\beta| = \omega_{HF}$ in the weak coupling case, and $\omega_\alpha + \omega_\beta = \omega_{HF}$ for the strong coupling case. The frequency ω_{HF} is solely

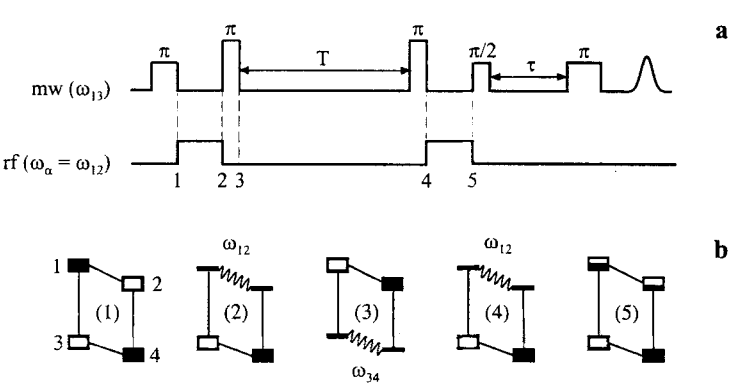

Fig. 2. HYEND. **a** Pulse sequence, **b** evolution of the states in a two-spin system *SI* (adapted from ref. 27).

determined by the hyperfine coupling. The resulting echo signal is proportional to $C_{HF}^{\alpha/\beta}\sin(\omega_{HF}T + \phi_{HF}^{\alpha/\beta}) + O(T)$ with amplitude and phase factors which depend on the hyperfine interaction. Combination and fundamental frequencies are described by the term $O(T)$ [26].

Recently HYEND was applied to resolve hfis in the rhodaazacyclopropane radical cation $[Rh(trop_2NCH_2)(PPh_3)]^+$ [28]. It is a small strained hydrocarbon molecule stabilized by a rhodium ion incorporated in the three-membered ring. Strained hydrocarbons are known to have remarkably low oxidation potentials and an intriguing question was to see if this property could be realized by incorporating the transition metal in a small strained ring. The carbon of the methylene bridge, amine nitrogen, and the rhodium ion form a triangle: Rh-C-N [28]. To reveal the hyperfine couplings of rhodium and carbon, ENDOR spectroscopy was used on a ^{13}C-enriched complex. However, Davies ENDOR spectra recorded across the field-swept EPR spectrum show broad, badly resolved patterns from many overlapping lines, even when the proton signals were suppressed by semiselective mw pulses (as an example see the spectrum shown in Fig. 3a which was recorded at an observer position close to $g_\perp$). HYEND enabled the carbon and rhodium signals to be resolved (Fig. 3b). The two contributions appeared as ridges along straight lines with a slope of 1/2 as a function of ν_{HF}, and separated in the ENDOR dimension by double the nuclear Larmor frequencies of either ^{13}C or ^{103}Rh. The slope 1/2 comes from the magnetic quantum number m_S which gives Am_S in the ENDOR dimension and $A \times \Delta m_S$ in the hyperfine one. The signals between the rhodium nuclear Zeeman lines at $\nu_{ENDOR} = \nu_{HF}/2$ are interpreted as due to a sign change in the hfi **A** =

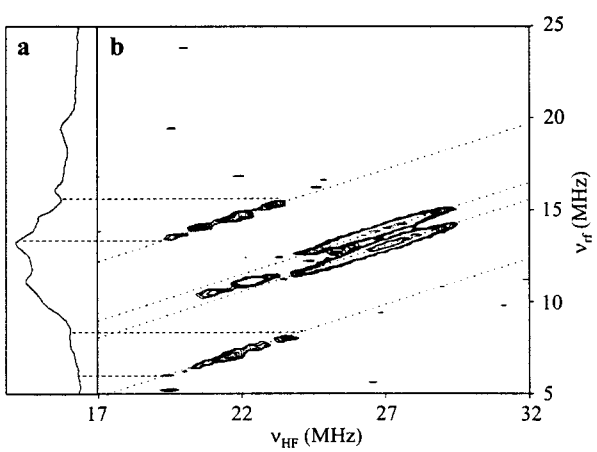

Fig. 3. ENDOR of the ^{13}C-enriched rhodaazacyclopropane cation measured at a field position around $g_\perp$. **a** Davies ENDOR spectrum obtained with nonselective mw pulses; **b** HYEND spectrum showing the correlation ridges attributed to the carbon and rhodium nuclei. ν_{HF} is the sum of nuclear frequencies in the two electron spin manifolds. The dashed lines select the area in the ENDOR spectrum **a** with carbon signals. The dotted straight lines in **b** have the slopes 1/2 and are separated in the rf dimension by twice the Larmor frequency of the corresponding nucleus.

(29, 25, −18) MHz. Another way to have selectivity in the hyperfine dimension is provided by polarization-based hyperfine-selective ENDOR with field jumps [29].

Other new techniques that were developed, a pulse version of TRIPLE-ENDOR, multiple-quantum ENDOR, time-domain ENDOR and coherence transfer ENDOR, are reviewed in refs. 20 and 22. The story with simultaneous excitation of the nuclear transitions in both electron spin manifolds is completed with time-domain ENDOR employing chirp rf pulses [30]. In this approach, nuclear coherences are created in a wide frequency range (i.e., NCs in both electron spin manifolds are created) using an rf pulse where the rf frequency is swept during the pulse. The desired nuclear spectrum is obtained by allowing the NCs to evolve in time, converting them back to polarizations, and applying a Fourier transform to the resulting modulated echo trace. The nuclear frequencies axis has a high resolution that is limited by T_{1e} and T_{2n}, and the sensitivity is improved due to the broad-band excitation.

4 RF-Driven ESEEM

The extremely successful ESEEM method fails in the case of an electron-nuclear system with isotropic interactions, as an example for radicals in solution. To exploit the ESEEM effect in this situation, an rf-driven approach has been proposed [31]. It was shown that the nonsecular hyperfine contribution, which is responsible for the ESEEM effect, can be reintroduced using an rf field that is continuously acting on the spin system during the pulse sequence. Indeed, in both cases the nuclear states are coupled, via either dipolar coupling or an rf field.

The spin Hamiltonian for a two-spin system $S = 1/2$, $I = 1/2$ in the laboratory frame and including an rf field can be written as [31]

$$\mathcal{H} = \omega_S S_z + a\mathbf{S}\cdot\mathbf{I} - \omega_I I_z + (2\Omega_{2S}S_x - 2\Omega_{2I}I_x)\cos(\omega_{rf}t)\,, \tag{5}$$

where $2\Omega_{2S/2I}$ is the amplitude of an oscillating rf field seen by the electron and nucleus. Transforming Eq. (5) to a doubly rotating frame using $R = \exp(-i(\omega_S S_z - \omega_{rf}I_z)t)$ and $\mathcal{H}_{DR} = R^{-1}\mathcal{H}R - iR^{-1}dR/dt$, applying average Hamiltonian theory [32], and neglecting the minor terms of order Ω_I/ω_I, one obtains a time-independent spin Hamiltonian which describes the desired effect [31]

$$\mathcal{H}_{rf} \approx \Omega_I I_z + aS_z I_z - \Omega_{2I}I_x + \frac{a\Omega_{2I}}{\omega_I}S_z I_x\,. \tag{6}$$

The last two terms in Eq. (6) represent nonsecular contributions induced by the rf field. A formula for the two-pulse electron spin echo modulation resulting from Eq. (6) is identical to the conventional case [33] but with a modulation depth k and fundamental ESEEM frequencies $\omega_{\alpha/\beta}$ which are functions of the rf frequency

and the rf amplitude. If the rf is resonant with one unperturbed nuclear transition, $\omega_{rf} = \omega_I \pm a/2$, and $a \gg \Omega_{2I}$ the simplified equations for these quantities are [31]

$$k \approx 1 - \frac{\Omega_{2I}^2(\omega_I \mp a/2)^2}{a^2\omega_I^2},$$

$$\omega_{\alpha/\beta} = \left(a^2 + \Omega_{2I}^2 \left(1 \mp \frac{a}{2\omega_I} \right)^2 \right)^{1/2}, \tag{7}$$

$$\omega_{\beta/\alpha} = \Omega_{2I} \left(1 \pm \frac{a}{2\omega_I} \right)^2. \tag{8}$$

Equation (8) describes the frequency of a nuclear transition on resonance with the rf field in one of the electron spin manifolds, and Eq. (7) gives the eigenfrequency in the other electron spin manifold. In any case, one of the two fre-

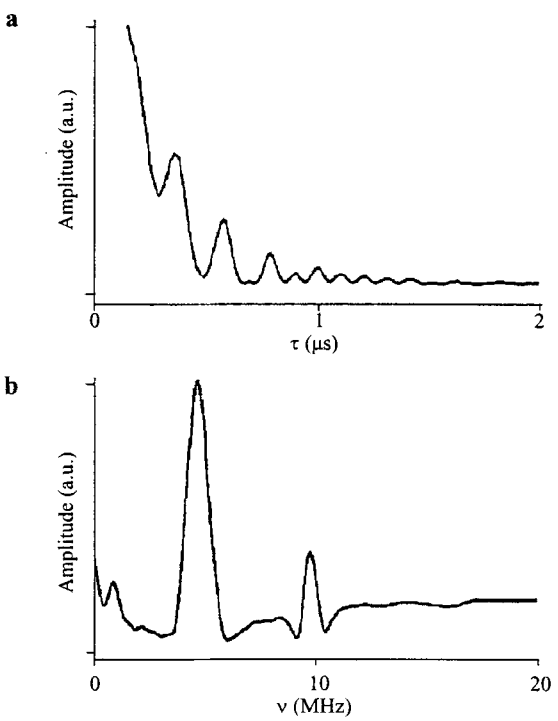

Fig. 4. Two-pulse rf-driven ESEEM of the tri-*t*-butylphenoxyl radical in mineral oil. **a** Time-domain trace, and **b** cosine Fourier transformation showing fundamental and combination nuclear frequencies in the α electron spin manifold. An rf irradiation with a frequency of 16.4 MHz with a field strength of 0.5 MHz was used (adapted from ref. 31).

quencies is close to zero, and the other one is close to the isotropic coupling *a*. Figure 4 shows an example of rf-driven two-pulse ESEEM on the tri-*t*-butylphenoxyl radicals in mineral oil. The spectrum (Fig. 4b) contains the expected peaks in accordance with Eqs. (7) and (8). Further developments in this direction are described in ref. 7.

5 Bridged Loop-Gap ENDOR Resonator

An innovative breakthrough in the ENDOR resonator design has been achieved by introducing a version of the loop-gap resonator [34] which is transparent to rf fields. In this version thin metallic layers placed on the inner surface of a quartz tube have been used to construct two inductive half-loops, and capacitive bridges between them were created on the outer surface of the tube, giving the name for the structure, bridged loop-gap resonator (BLGR) [35]. For ENDOR operation, a solenoid rf coil surrounds the BLGR with the coil axis parallel to the resonator axis. This idea is somewhat counter to the more popular tactic of placing an rf coil inside the resonator to obtain the highest rf field at the sample position. Nevertheless, the coil diameter in the BLGR scheme is about 10 mm, which is very similar to the corresponding cw X-band ENDOR cavity-based resonators (e.g., EN801 from Bruker BioSpin). Since there are no closed loops perpendicular to the rf field the eddy currents are minimized. A low quality factor also contributes to make the resonance condition stable. This facet in combination with the high sensitivity of the loop-gap structure makes the ENDOR BLGR a near optimal combination for pulse ENDOR at X-band frequencies.

The setup, which incorporates a BLGR with an ENDOR coil (as well as modulation or field jump coils), is shown in Fig. 5a. The rf π-pulse for the protons in a tuned version was as short as 1 μs as determined from the nutation data shown in Fig. 5b. The rf field strength of 20 mT in a tuned version (1–25 MHz) and 2 mT for a broad-band setup (1–200 MHz) was obtained with an rf power of 2 kW. For the former case a transformer unit has been developed which keeps automatically matching the circuit over the frequency range. The high performance and simplicity of the ENDOR BLGR was successfully used in ref. 36. To optimize the mw performance of the BLGR, the structure was emulated numerically [37] by the MAFIA program (the first commercial package for electromagnetic field simulations [38]). Recently, a Q-band loop-gap resonator was tailored for single-electron-spin spectroscopy by using the newest version of the program [39].

6 Pulse ENDOR Applications at Q-Band

In the new millennium, pulse ENDOR techniques continue to spread over the research institutes and the application areas [40]. In particular, pulse ENDOR became a routine experiment at X-band, is well exploited at W-band, and pulse

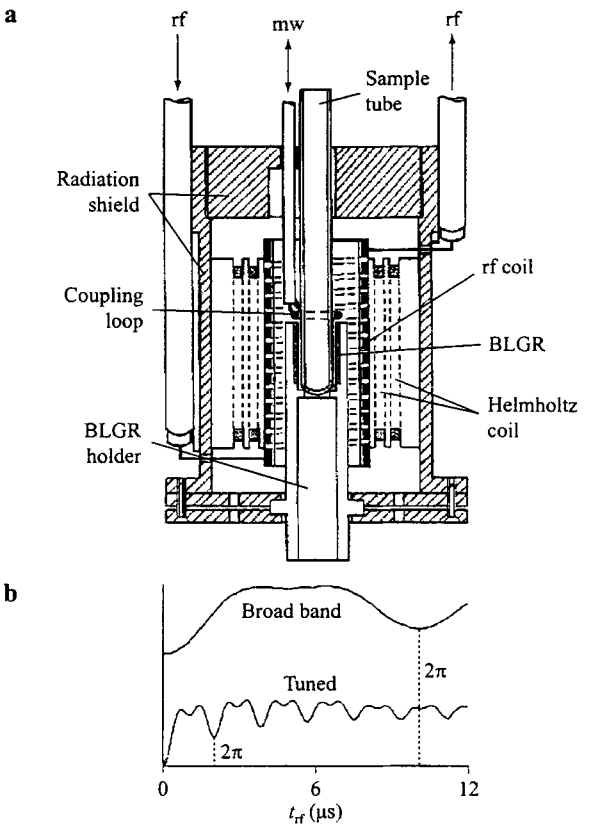

Fig. 5. BLGR for pulse ENDOR operation. **a** Cross section of the resonator assembly. **b** Nutations of two protons in the copper complex resonant at about $\nu_{rf} = 19$ MHz (enhancement factor of 1.4) obtained with an rf pulse of 2 kW using a broad band and a tuned rf circuit with $\nu_{rf} \neq \nu_{match}$ (adapted from ref. 35).

Q-band applications have started to grow up due to the appearance of powerful spectrometers [41, 42]. Representative Q-band examples include an unraveling of the copper binding sites in the terminal domain of the prion protein [43, 44]; cobalt ENDOR of an oxygenated cobalt(II) corrin complex [45]; and ^{2}H and ^{13}C ENDOR of a cobalt(IV) corrole complex [46].

The well-adopted strategy in pulse EPR is to measure ENDOR at different field positions across the field-swept EPR spectrum and simulate the obtained spectra with the expected field dependence (and check the expectation) taking into account orientation selectivity. The latter usually depends on the *g*-factor anisotropy and consequently increases with increasing mw frequency. However, there are two negative effects that occur as the mw frequency increases (not technical in nature) which constrain the spectroscopists. Firstly, the sensitivity diminishes as the resolution (mw frequency) increases, which is partially com-

pensated for by a sensitivity rise with mw frequency (because of larger mw quanta and higher polarization). Secondly, there is a decrease in the hyperfine enhancement factor [33] which can make ENDOR difficult on nuclei with low gyromagnetic ratios that have relatively large hyperfine couplings. Both constraints are essential in disordered systems containing transition metal complexes in low concentrations. These considerations, and the lower technical demand compared to higher-frequency spectrometers [47], make Q-band very attractive for EPR specialists. Indeed, frequently the resolution of nuclear frequencies is already satisfactory at Q-band. In particular, at Q-band the separation of different nuclear contributions in the spin Hamiltonian is often achieved. In the case of an $I = 1$ nucleus and strong coupling, the condition for the separation can be written as $A > 2\omega_I > 3P_z$, where the last quantity is the largest principal value of the nuclear quadrupole tensor. This inequality is, for example, fulfilled at Q-band for most paramagnetic complexes with ^{14}N nuclei (as an example see Fig. 6). The separation of different nuclei is often excellent at Q-band, where the proton signals are centered around ca. 55 MHz and usually well separated from signals due to strongly coupled nuclei like N, S, P and C. To illustrate the ability of this frequency range a few interesting examples follow.

Recently, the porphyrin family has been extended with a new member, an N-confused tetraphenyl porphyrin (nctpp, also known as "inverted" porphyrin) [48]. This porphyrin isomer retains the molecular backbone of the regular porphyrin but contains a "confused" pyrrole ring with one pyrrolic C-H group point-

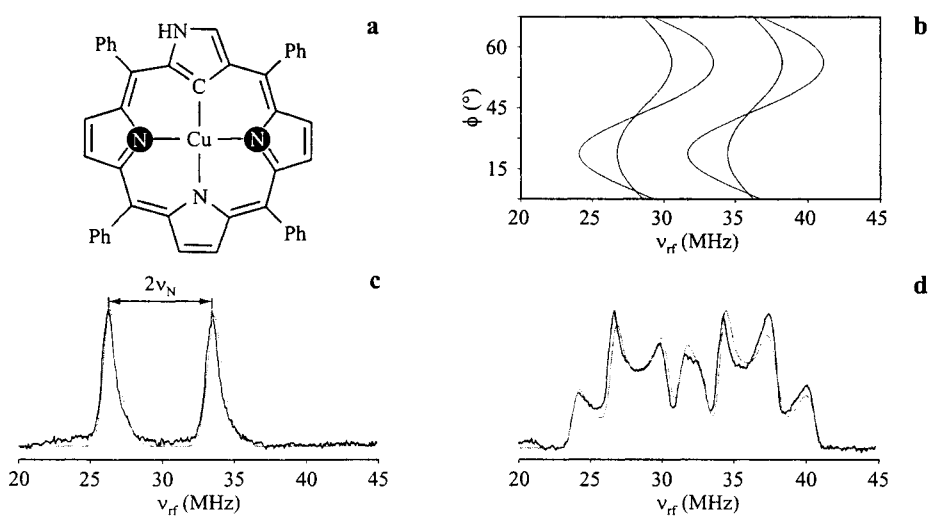

Fig. 6. Q-band ENDOR of copper(II) N-confused tetraphenyl porphyrin. **a** Sketch of the molecule with the nitrogens under study highlighted. **c** and **d** Spectra measured at $g_{\parallel}$ (**c**) and $g_{\perp}$ (**d**) positions. The corresponding magnetic fields are perpendicular and parallel to the porphyrin plane. Black traces are experimental spectra, and grey traces are simulations. **b** Calculated orientational dependence of the nuclear frequencies in the porphyrin plane (adapted from ref. 49).

ing into the microcycle (Fig. 6a). The nctpps form stable organometallic complexes with many transition metal centers and have the ability to act as a neutral to trianionic ligand. The ligand can stabilize uncommon spin and oxidation states of various metal ions thereby forming a carbon–metal bond. They are thus of considerable interest in chemistry [48].

Recently an asymmetric spin density distribution in the Cu^{II} N-confused tetraphenyl-porphyrin has been reported [49]. In particular, the spin density on the nitrogens N1 and N2 (Fig. 6a) was obtained with the help of ENDOR. The Q-band Davies ENDOR spectra measured at observer positions close to $g_{||}$ (Fig. 6c) and $g_{\perp}$ (Fig. 6d) demonstrate a well-resolved structure. The spectrum recorded near to $g_{||}$ consists of a doublet split by $2\nu_{14N}$ and centered around $\nu_{rf} = 30$ MHz. The nuclear quadrupole splitting along this orientation is unresolved, whereas it is clearly visible upon changing the observer position to $g_{\perp}$. The hyperfine couplings were found to be higher than in the conventional copper tetraphenyl porphyrin and the principal values of the hfi and nuclear quadrupole interactions are $\mathbf{A} = (71.5, 58.3, 59.5)$ MHz and $\mathbf{P} = (-0.87, 1, -0.13)$ MHz, respectively. The latter parameters were obtained by simulation of observed spectra using the EasySpin package [50]. The nuclear quadrupole contribution was obtained with good accuracy due partially to the good separation of the nuclear quadrupole and nuclear Zeeman contributions achieved at Q-band. The orientation dependence of the nuclear frequencies in the porphyrin plane, shown in Fig. 6b, demonstrates that maxima in the spectra appear at the turning points in the angular dependence of the nuclear quadrupole splitting.

The next example is related to one of the largest biological processes in the world, the conversion of substrates such as H_2/CO_2, acetate, formate or methanol to methane. In this process methylcoenzyme M reductase (MCR) serves methanogenic bacteria in the formation of methane by catalyzing the reaction of methylcoenzyme M (CH_3-S-CoM) with coenzyme B (HS-CoB) to methane and CoM-S-S-CoB. This process is responsible for the largest part of the annual emission (estimated $5 \cdot 10^8$ t/year) of this very effective greenhouse gas into the atmosphere. MCR has the nickel cofactor F_{430} at its active site as is shown in Fig. 7a. The enzyme exists in various oxidation and spin states, for example: MCR_{red2} (Ni^{I}, d^9, Ni-sulfur bond), MCR_{ox1} (the thiolate Ni^{III}-$^{-}$SR in resonance with Ni^{II}-$^{-}$SR, a thiyl radical/high-spin $S = 1$ Ni^{II} complex) and MCR_{BPS} (Ni-alkyl species formed after reaction with the irreversible inhibitor 3-bromopropane sulfonate) [51–53]. Here we take as an illustrative example a Davies ENDOR spectrum from the MCR_{ox1} complex which displays ^{61}Ni and hydropyrrolic nitrogen signals (Fig. 7b). The ^{61}Ni ($I = 3/2$) peaks are centered at approximately half the hyperfine coupling, 40 MHz/2, split by twice the nuclear Zeeman frequency (2×3.8 MHz), and split by twice the nuclear quadrupole splitting (the calculated nuclear frequencies are 29, 25 and 19 MHz in one electron spin manifold, and 20, 17 and 10 MHz in the other, $|\mathbf{A}| = (39, 42, 132)$ MHz, $|e^2qQ/h| = 22$ MHz). Nuclear frequencies from the four hydropyrrolic nitrogens are between 5 and 20 MHz.

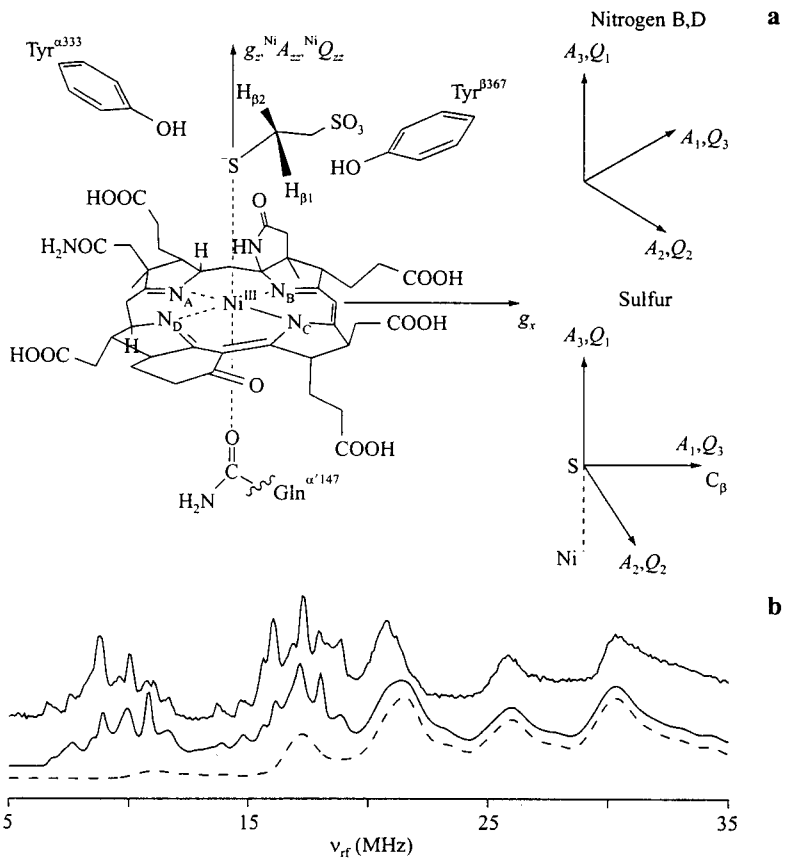

Fig. 7. **a** Schematic representation of F_{430} and the orientation of the g-matrix and the **A** and **Q** axes for ^{61}Ni, ^{33}S and ^{14}N. **b** Q-band (35.3 GHz) Davies ENDOR spectra of ^{61}Ni-MCR$_{ox1}$ measured near to $g_{\parallel}$. The traces from top to bottom: experimental, simulated sum of ^{14}N and ^{61}Ni spectra; simulated ^{61}Ni contribution only (adapted from ref. 52).

7 Multiple-Photon Transitions in EPR

A linearly polarized oscillating field can be considered as a superposition of right- and left-hand circularly polarized fields which consist of photons with positive (σ^+) and negative (σ^-) helicity, respectively [54]. These circular components have projections of their angular moments $\pm n\times\hbar$, where n is the photon number. In electron paramagnetic resonance of a two-level system ($S = 1/2$) with an mw field perpendicular to the static magnetic field, the mw $\sigma^{\pm}$ field exchanges its moment with an electron spin when the energy conservation rule is fulfilled. When an oscillating linear magnetic field, $\pi = (\sqrt{2}/2)\sigma^+ + (\sqrt{2}/2)\sigma^-$, is parallel to the static field, no resonances are expected if the electron Zeeman interaction is fully isotropic. Nevertheless, this consideration is oversimplified and a resonance pic-

ture can be more complicated. In particular, multiple-photon transitions can easily be observed in EPR (reviewed in ref. 5).

Here we consider a particular kind of multiple-photon transition of the type $\sigma + k\times\pi$ ($k\in\mathbb{Z}$), where a single σ mw photon and multiple π rf photons are absorbed and emitted by the $S = 1/2$ spin system. Alternatively, these transitions can be considered as the EPR transitions between the states of an electron spin dressed by a longitudinal rf field. We will use the latter approach and exploit the elegant Floquet theory [55] to show how the dressing rf field influences the spin system. In a rotating wave approximation, for the mw field, the spin Hamiltonian of an $S = 1/2$ system with a longitudinal rf field $\Omega_2\cos(\omega_2 t)$ can be written as

$$\mathcal{H} = \Omega_S S_z + \Omega_1 S_x + \Omega_2 \cos(\omega_2 t) S_z, \tag{9}$$

where $\Omega_S = \omega_S - \omega_{mw}$ is a resonance offset and Ω_1 is an mw field amplitude. Its corresponding time-independent Floquet analog can be built using the following equation for the matrix elements [56]:

$$\langle \alpha n \mid \mathcal{H}_F \mid \beta m \rangle = \langle \alpha \mid \mathcal{H}^{n-m} \mid \beta \rangle + n\omega_2 \delta_{\alpha\beta}\delta_{nm},$$

where $|\gamma l\rangle$ represents a Floquet state with the index γ for the magnetic quantum number and l is the index of a component in the Fourier series expansion of the spin Hamiltonian $\mathcal{H}$. $\mathcal{H}^{n-m}$ is the corresponding Fourier coefficient, and ω_2 is a frequency displacement. For the case in hand, the DC and first harmonics only are present in the Fourier expansion. A matrix representation of the Floquet Hamiltonian can easily be constructed:

$$\mathcal{H}_F = E_{\mathbb{N}} \otimes \mathcal{H}^0 + E^{\pm 1}_{\mathbb{N}} \otimes \mathcal{H}^1 + \omega_2(\mathbb{N} \otimes E_S), \tag{10}$$

where matrices on the left-hand side in direct products have the dimension of Fourier space $\mathbb{N} = (-n, -n+1, \ldots, n)$ and those on the right-hand side are in spin space. Upper indices of the unity matrix $E^{\pm 1}_{\mathbb{N}}$ mean that it has ones on the diagonal adjacent to the main one. To illustrate the property of such states, let us calculate the transition probability between the eigenstates of Eq. (10). This can be done by numerical diagonalization and calculating the scalar product of its eigenvectors. The inset in Fig. 8 shows the probabilities as a function of the longitudinal field strength Ω_2 under the conditions $\omega_2 = 1$, $\Omega_1 = 0.1$ and assuming a homogeneous line width $\delta\Omega_S = 0.2$ (i.e., $\Omega_1 < \delta\Omega_S < \omega_2$). The spectra have two peculiarities: sidebands displaced by $n\omega_2$ with respect to the exact resonance of bar spins, $\Omega_2 = 0$ at $\Omega_S = 0$. Secondly the line intensity changes with Ω_2 quasi-periodically. Closer analysis shows that the intensity follows to the Bessel functions of the first kind with an order which coincides to $n = \Omega_S/\omega_2$. As is shown in Fig. 8, the intensity of the central line at $n = 0$ and the first two sidebands at $n = \pm 1$ follows to the function $J_n(z)^2$ with argument $z = \Omega_2/\omega_2$. The positions

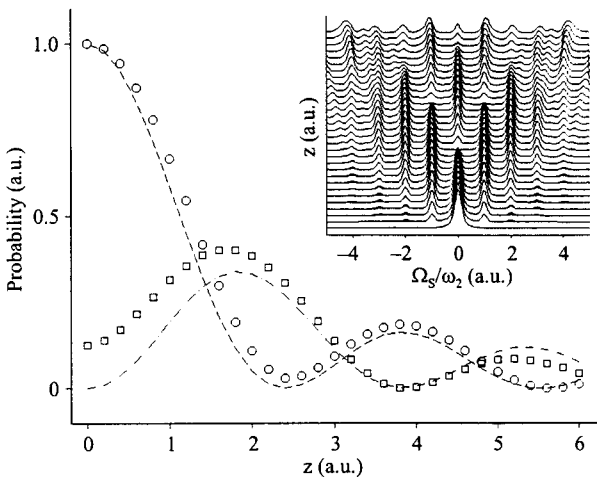

Fig. 8. Mw transition probability for a $S = 1/2$ spin system excited by a longitudinal rf field as a function of the ratio between rf field strength and frequency $z = \Omega_2/\omega_2$. Inset shows sidebands induced by the rf field. The circles are the intensity of the central band at resonance offset $\Omega_S = 0$, and the squares represent the intensity of the sidebands at $\Omega_S = \pm 1\omega_2$. The dashed and dot-dashed lines are the squared Bessels functions with argument z (not a fit).

of maxima and minima coincide well with zeros of the corresponding Bessel functions ($J_0(z) = 0$ at $z = 2.41$, 5.52, ... and $J_{\pm 1}(z) = 0$ at $z = 3.83$, ...). The small deviations in the functional dependence are due partially to the simplicity of the used model, and the extra intensity at $n = \pm 1$ for small z is due to contamination by the wings of the central line.

The influence of a longitudinal field modulation on the shape of spectral lines has been studied in great detail, because it was, and still is, implemented in order to increase the sensitivity of cw EPR or cw NMR spectrometers. The existence of sidebands and their scaling with Bessel functions is well known (see ref. 57). However, the observed peculiar properties can be used in pulse EPR. The theoretical description above was related to cw spectroscopy. In the pulse case we are interested more in transition amplitudes than in probabilities. A vanishing of the resonance lines shown in the inset of Fig. 8 can be explained by transforming the spin Hamiltonian in Eq. (9) using $R = \exp[i(k\omega_2 t + z\sin\omega_2 t)S_z]$ to a toggling frame [5]

$$\mathcal{H}_{\text{tog},k} = (\Omega_S - k\omega_2)S_z + J_{-k}(z)\Omega_1 S_x + \mathrm{O}(t).$$

In this frame it is clearly visible that the longitudinal rf field modulates an effective mw field for the kth sideband; again the Bessel function of the corresponding order appeared as a scaling factor. Thus the effective mw field seen by the electron spin is zero for a certain sideband (or central band) at a certain rf field amplitude and no EPR transition is observed.

The next example demonstrates how longitudinal rf fields can influence the primary electron spin echo amplitude (Fig. 9a). In the conventional case the echo amplitude depends on the flip angles of the mw pulses as $\sin(\Omega_1 t_{p1})\sin^2(\Omega_1 t_{p2}/2)$ [33]. In the dressed spin case, with the longitudinal rf field (at frequency $\omega_2/2\pi = 5$ MHz) superimposed on the first mw pulse in the sequence, a $\sin(J_0(z)\pi/2)$ variation of the echo amplitude was observed (Fig. 9a). The rf field strength was calibrated using a proton ENDOR experiment (at about 15 MHz) and then extrapolated to 5 MHz. The observed zero crossing positions differ from the prediction by less than two percent. The disappearance of the echo signal demonstrates that the spin system can be made transparent to the mw irradiation [58]. This transparency can be controlled within a relatively broad spectral width. A second example is shown in Fig. 9b. The electron spin echo is created by "cutting" the mw field of a single long mw pulse and leaving just small slices at the beginning and end. The use of the transparency effect in a practical application has been demonstrated in four-pulse double electron-electron resonance (DEER) [59]. As is shown

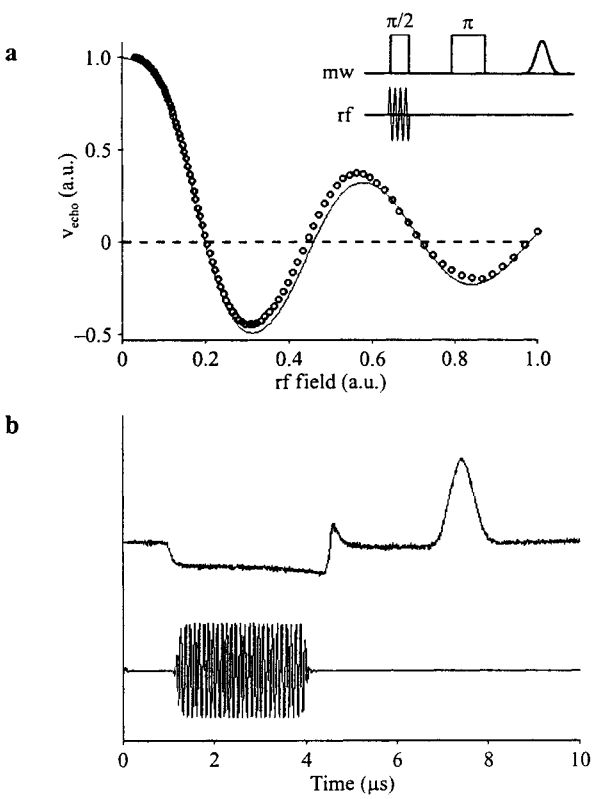

Fig. 9. Primary electron spin echoes. **a** Echo amplitude as a function of dressing rf field strength. **b** Creation of the echo by making the spin system transparent to mw irradiation during a longitudinal rf pulse with a strength 2.4 times larger than its frequency.

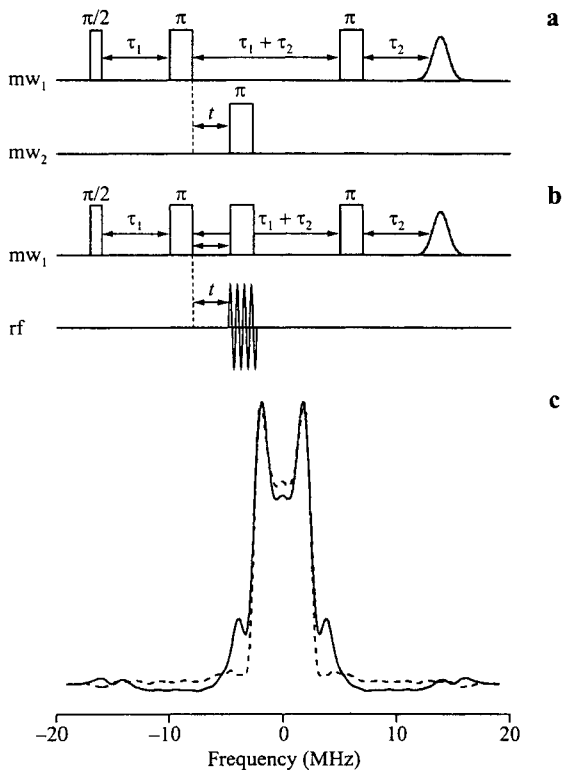

Fig. 10. Practical application of the transparency effect in DEER. **a** Conventional four-pulse DEER sequence. **b** Four-pulse DEER without second mw frequency. **c** Dipolar spectra of nitroxide biradical measured with sequence **a** (dashed line) and **b** (solid line) (adapted from ref. 60).

in Fig. 10b, the second mw frequency ω_{mw2} used in the original sequence (Fig. 10a) is in essence replaced by a "bichromatic" pulse with frequencies ω_{mw1} and ω_{rf} [60]. Figure 10c shows the dipolar spectra obtained using this sequence and conventional four-pulse DEER, the concurrence is excellent.

8 Conclusion

This review has concentrated on traditional and special applications of rf fields in EPR spectroscopy. Many of the methods were inspired by Arthur Schweiger and developed in the EPR group at ETH. Numerous contributions to ENDOR/EPR spectroscopy were considered in detail to provide the reader with a picture of important effects or methods which can be exploited in this area. They are the implementation of circularly polarized rf fields in ENDOR, pulse ENDOR methodology, rf-driven ESEEM, BLGR, pulse ENDOR at Q-band, and multiple-photon transitions in EPR. Some techniques were mentioned only briefly, as, for example, time-domain ENDOR. Low-frequency experiments which use magnetic

field jumps or wiggling were not included at all. For a comprehensive description of these experiments and the field of pulse EPR in general we recommend the fundamental book for pulse EPR by Schweiger and Jeschke [33].

Acknowledgments

We express our deepest gratitude to Arthur Schweiger for his inspiring leadership and insight, both on a scientific and personal level. We greatly appreciate the support and contributions from the current and former ETH group members, in particular from Stefan Stoll, Inés García Rubio, Dariush Hinderberger, George Mitrikas, Sreekanth Anandaram, Carlos Calle, Besnik Kasumaj, Patrick Léger, Maria Grazia Santangelo, Jörg Forrer, René Tschaggelar, Bruno Mancosu, Irène Müller, Cinzia Finazzo, Barbara Feurer, Matvey Fedin, Moritz Kälin, Walter Lämmler, Rüdiger-Albert Eichel, Lorenz Liesum, Josef Granwehr, Willi Groth, Zoltan Mádi, Sabine Van Doorslaer, Rainer Bachmann, Johan J. Shane, Pol Schosseler, and Gustavo Sierra. We acknowledge the long-term support provided by the Swiss National Science Foundation.

References

1. Feher G.: Phys. Rev. **103**, 834–835 (1956)
2. Mims W.B.: Proc. R. Soc. Lond. A **283**, 452–457 (1965)
3. Davies E.R.: Phys. Lett. A **47**, 1–2 (1974)
4. Jeschke G.: Chem. Phys. Lett. **301**, 524–530 (1999)
5. Kälin M., Fedin M., Gromov I., Schweiger A. in: Novel NMR and EPR Techniques. Lecture Notes in Physics, vol. 684 (Dolinšek J., Vilfan M., Žumer S., eds.), pp. 143–183. Berlin: Springer 2006.
6. Mims W.B.: Phys. Rev. B. **5**, 2409–2419 (1972)
7. Kälin M., Schweiger A.: J. Chem. Phys. **115**, 10863 (2001)
8. Abragam A., Bleaney B.: Electron Paramagnetic Resonance of Transition Ions. Oxford: Clarendon Press 1970.
9. Kevan L., Kispert L.D.: Electron Spin Double Resonance Spectroscopy. New York: Wiley-Interscience 1976.
10. Schweiger A.: Struct. Bonding **51**, 1–119 (1982)
11. Schweiger A., Günthard H.H.: Mol. Phys. **42**, 283–295 (1981)
12. Forrer J., Schweiger A., Berchten N., Günthard H.H.: J. Phys. E: Sci. Instrum. **14**, 565–568 (1981)
13. Schweiger A., Günthard H.H.: Chem. Phys. **70**, 1–22 (1982)
14. Schweiger A., Rudin M., Forrer J., Günthard H.H.: J. Magn. Reson. **50**, 86–94 (1982)
15. Dinse K.P., Biehl R., Möbius K.: J. Chem. Phys. **61**, 4335–4341 (1974)
16. Schweiger A., Günthard H.H.: J. Magn. Reson. **57**, 65–78 (1984)
17. Schweiger A., Rudin M., Günthard H.H.: Mol. Phys. **41**, 63–74 (1980)
18. Rudin M., Schweiger A., Günthard H.H.: J. Magn. Reson. **51**, 278–285 (1983)
19. Rudin M., Forrer J., Schweiger A.: J. Magn. Reson. **54**, 447–457 (1983)
20. Schweiger A.: Angew. Chem. Int. Ed. **30**, 265–292 (1991)
21. Sörensen O.W., Eich G.W., Levitt M.H., Bodenhausen G., Ernst R.R.: Prog. NMR Spectrosc. **16**, 163 (1983)
22. Gemperle C., Schweiger A.: Chem. Rev. **91**, 1481–1505 (1991)
23. Kurreck H., Kirste B., Lubitz W.: Electron Nuclear Double Resonance Spectroscopy of Radicals in Solution. New York: VCH 1988.
24. Epel B., Arieli D., Baute D., Goldfarb D.: J. Magn. Reson. **164**, 78–83 (2003)
25. Deblon S., Liesum L., Harmer J., Schonberg H., Schweiger A., Grutzmacher H.: Chem. Eur. J. **8**, 601–611 (2002)

26. Jeschke G., Schweiger A.: Chem. Phys. Lett. **246**, 431–438 (1995)
27. Jeschke G.: New Concepts in Solid-State Pulse Electron Spin Resonance. PhD. thesis ETH nr. 11873. Zurich: Swiss Federal Institute of Technology 1996.
28. Maire P., Sreekanth A., Buttner T., Harmer J., Gromov I., Ruegger H., Breher F., Schweiger A., Grutzmacher H.: Angew. Chem. Int. Ed. **45**, 3265–3269 (2006)
29. Buhlmann C., Schweiger A., Ernst R.R.: Chem. Phys. Lett. **154**, 285–291 (1989)
30. Jeschke G., Schweiger A.: J. Magn. Reson. A **119**, 45–52 (1996)
31. Cho H., Pfenninger S., Forrer J., Schweiger A.: Chem. Phys. Lett. **180**, 198–206 (1991)
32. Waugh J.S. in: Encyclopedia of Nuclear Magnetic Resonance (Harris R.K., ed.), vol. 2, p. 849. Chichester: Wiley 1996.
33. Schweiger A., Jeschke G.: Principles of Pulse Electron Paramagnetic Resonance. New York: Oxford University Press 2001.
34. Froncisz W., Hyde J.S.: J. Magn. Reson. **47**, 515–521 (1982)
35. Forrer J., Pfenninger S., Eisenegger J., Schweiger A.: Rev. Sci. Instrum. **61**, 3360–3367 (1990)
36. Shane J.J., Gromov I., Vega S., Goldfarb D.: Rev. Sci. Instrum. **69**, 3357–3364 (1998)
37. Pfenninger S., Forrer J., Schweiger A., Weiland T.: Rev. Sci. Instrum. **59**, 752–760 (1988)
38. Dehler M., Dohlus M., Fischerauer A., Fischerauer G., Hahne P., Klatt R., Krawczyk F., Propper T., Schutt P., Weiland T., Ebeling F., Marx M., Wipf S.G., Steffen B., Barts T., Browman J., Cooper R.K., Rodenz G., Rusthoi D.: IEEE Trans. Magn. **26**, 751–754 (1990)
39. Simovic B., Studerus P., Gustavsson S., Leturcq R., Ensslin K., Schuhmann R., Forrer J., Schweiger A.: Rev. Sci. Instrum. **77**, 064702 (2006)
40. Van Doorslaer S., Schweiger A.: Naturwissenschaften **87**, 245–255 (2000)
41. Davoust C.E., Doan P.E., Hoffman B.M.: J. Magn. Reson. **119**, 38–44 (1996)
42. Gromov I., Shane J., Forrer J., Rakhmatullin R., Rozentzwaig Y., Schweiger A.: J. Magn. Reson. **149**, 196–203 (2001)
43. Van Doorslaer S., Cereghetti G.M., Glockshuber R., Schweiger A.: J. Phys. Chem. B **105**, 1631–1639 (2001)
44. Cereghetti G.M., Schweiger A., Glockshuber R., Van Doorslaer S.: Biophys. J. **81**, 516–525 (2001)
45. Van Doorslaer S., Schweiger A., Krautler B.: J. Chem. Phys. B **105**, 7554–7563 (2001)
46. Harmer J., Van Doorslaer S., Gromov I., Schweiger A.: Chem. Phys. Lett. **358**, 8–16 (2002)
47. Allgeier J., Disselhorst J.A.J.M., Weber R.T., Wenckebach W.T., Schmidt J. in: Modern Pulsed and Continuous-Wave Electron Spin Resonance (Kevan L., Bowman M.K., eds.), pp. 267–283. New York: Wiley 1990.
48. Latos-Grazyński L. in: The Porphyrin Handbook (Kadish K.M., Smith K.M., Guilard R., eds.), vol. 2, pp. 361–416. San Diego: Academic Press 2000.
49. Mitrikas G., Calle C., Schweiger A.: Angew. Chem. Int. Ed. **44**, 3301–3303 (2005)
50. Stoll S., Schweiger A.: J. Magn. Reson. **178**, 42–55 (2006)
51. Finazzo C., Harmer J., Jaun B., Duin E.C., Mahlert F., Thauer R.K., Van Doorslaer S., Schweiger A.: J. Biol. Inorg. Chem. **8**, 586–593 (2003)
52. Harmer J., Finazzo C., Piskorski R., Bauer C., Jaun B., Duin E.C., Goenrich M., Thauer R.K., Van Doorslaer S., Schweiger A.: J. Am. Chem. Soc. **127**, 17744–17755 (2005)
53. Hinderberger D., Piskorski R.R., Goenrich M., Thauer R.K., Schweiger A., Harmer J., Jaun B.: Angew. Chem. Int. Ed. **45**, 3602–3607 (2006)
54. Cohen-Tannoudji C., Dupont-Roc J., Grynberg G.: Atom-Photon Interactions. New York: Wiley 1992.
55. Levante T.O., Baldus M., Meier B.H., Ernst R.R.: Mol. Phys. **86**, 1195–1212 (1995)
56. Vega S. in: Encyclopedia of Nuclear Magnetic Resonance (Harris R.K., ed.), p. 2011. Chichester: Wiley 1996.
57. Haworth O., Richards R.E.: Prog. NMR Spectrosc. **1**, 1–14 (1966)
58. Kälin M., Gromov I., Schweiger A.: Phys. Rev. A **69**, 033809 (2004)
59. Pannier M., Veit S., Godt A., Jeschke G., Spiess H.W.: J. Magn. Reson. **142**, 331–340 (2000)
60. Fedin M., Kälin M., Gromov I., Schweiger A.: J. Chem. Phys. **120**, 1361–1369 (2004)

Authors' address: Igor Gromov, Laboratory of Physical Chemistry, ETH Zürich, HCI, 8093 Zürich, Switzerland
E-mail: gromov@esr.phys.chem.ethz.ch